

Cheng-peng Liu^{1,3}, Wen-ping Song^{1,3}, Shao-qiang Han² & Zhong-hua Han^{1,3}

¹School of Aeronautics, Northwestern Polytechnical University, Xi'an 710072, China
²Tianfu Engineering-oriented Numerical Software Innovation Center, College of Computer Science, Sichuan University, China
³National Key Laboratory of Aircraft Configuration Design, Xi'an 710072, China

Abstract

When rotorcrafts fly at high speeds, the retreating blades experience reverse flow due to their high advance ratio. Flow separates even at small angle of attack in reverse flow, which leads to negative lift, drag and pitching moment penalties. The aerodynamic characteristics of an airfoil are closely related to its geometric shape. Therefore, to mitigate aerodynamic deterioration caused by reverse flow and enhance the flight performance of rotorcrafts at high speeds, it is crucial to study the effects of geometric parameters on the aerodynamic characteristics of rotor airfoils in reverse flow. Given that conventional URANS method with low-precision scheme cannot adequately capture the vortex-induced large separation flow in reverse flow conditions, an improved high-order WENO scheme and IDDES method are used in airfoil reverse flow simulation. Initially, the simulation method is validated against experiment data of NACA 0012 airfoil in reverse flow. Subsequently, the OA312 airfoil is selected as a baseline and morphed by leading-edge radius, camber, camber crest position, thickness, thickness crest position and shape of trailing-edge. The aerodynamic coefficients of these modified airfoils are simulated and compared to analyze the influence of different geometry parameters. The results can be used to guide the design of new rotor airfoil with high performance.

Keywords: reverse flow, rotor airfoil, WENO scheme, IDDES

1. Introduction

The advance ratio of traditional rotocraft has been historically limited to $\mu=0.5$, one of the key limiting factor is reverse flow. In recent years, with the emergence of lift-offset coaxial configuration and slowed-rotor compound configuration, the advance ratio of rotorcraft has been greatly improved. However, these new configurations do not eliminate the occurrence of reverse flow [1]. On the contrary, due to high advance ratio and low rotor rotating speed, problems caused by reverse flow are more serious. At high advance ratio, free stream velocity at inboard sections of retreating blade exceeds rotating speed and air flows from airfoil's trailing-edge to leading-edge (See Figure 1a). This phenomena is called reverse flow. Flow separates even at small angle of attack in reverse flow, which leads to negative lift, drag and pitching moment penalties [2]. Under the alternating forward and reverse flow, the pressure center of the rotor airfoil changes periodically, resulting in blade pitching moment pulse, which may cause unsteady torsional load and stall flutter. These flow phenomena result in sharp deterioration of aerodynamic characteristics of rotor blades, and seriously restrict the increment of rotorcraft's forward flight performance.

The research of rotor airfoil in reverse flow is usually based on experiment and supplemented by numerical simulation. In term of experiment, Pope [3] and Leishman [4] conducted wind tunnel experiments of NACA 0015 airfoil and SC1095 airfoil at $0-360^{\circ}$ angle of attack, measured aerodynamic force coefficient and pressure distribution of these airfoils. Their work provided important reference

data for subsequent numerical simulation research. In recent years, Lind conducted a series experiments on NACA 0012 airfoil [1,5–8]. Lind studied the influence of trailing-edge shape on drag reduction, vortex shedding phenomena, unsteady load caused by aerodynamic hysteresis and Reynolds number effects on rotor blade section. However, limited by wind tunnel experiment condition, the Reynolds number in reverse flow experiment is typically below 10^6 , which do not cover the whole Reynolds number range encountered by rotor airfoil in real condition (See Figure 1b).

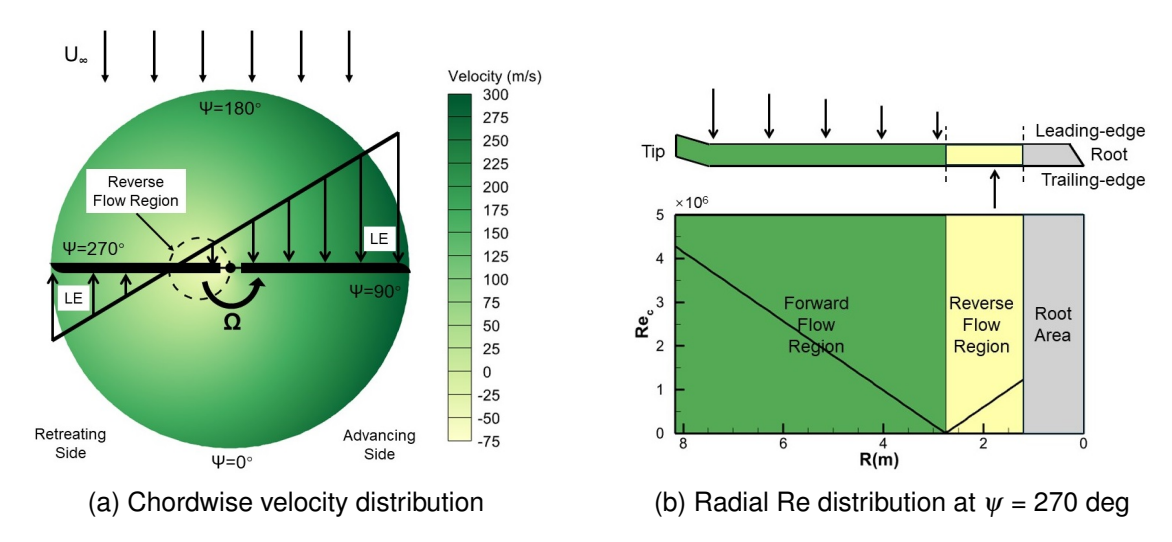


Figure 1 – Estimated velocity and Reynolds number distributions for an UH-60 rotor at Cruise Speed

Up to now, there have been very few numerical investigations on reverse flow. Smith [9] conducted numerical simulations of URANS and hybrid RANS/LES method on NACA 0012 and SC1095 aifoils at high and reverse angles of attack. Smith found that using hybrid RANS/LES simulation tubulence method results in a significant improvement in the ability of CFD to predict the characteristics of airfoils in these angles of attack region. Hodara [10] performed a collaborative experiment and CFD investigation of the aerodynamic behaviour of NACA 0012 airfoils in reverse flow. URANS method and DES method were used in Hodara's study. Jacobellis [2] performed computational and experimental investigation of camber-morphing airfoils to study the method of reducing drag in reverse flow for high-speed rotorcraft.

All of the researchers mentioned above indicates that the aerodynamic force calculated by URANS method compared well with experiment data at small angle of attack in reverse flow, but URANS method cannot accurately capture the complex vortex structure at large angle of attack. The pressure distribution showed obvious deviation at large angle of attack. URANS model will reach the limit of its predictive capabilities at about $\alpha_{rev} = -10^{\circ}$, and cannot reliably compute the massively separated boundary layer beyond this point [10]. A more advanced approach capable of capturing the 3D unsteady features of the flow is required. Moreover, the methods and mechanisms for reducing drag and improving aerodynamic performance of airfoils in reverse flow has not been fully studied. In this paper, IDDES method and 5^{th} -order WENO-K scheme [11] are applied to simulate rotor airfoil in reverse flow. The influence of rotor airfoil's geometry parameters on aerodynamic characteristics in reverse flow is studied, and the methods and mechanism of improving airfoil's aerodynamic characteristics in reverse flow by morphing its geometry parameters is revealed.

2. Methodology

2.1 Governing Equation

In this paper, an in-house structured CFD solver is used to calculate the force/moment coefficient of the rotor airfoils in reverse flow. The CFD solver solves Navier-Stokes (N-S) equation in generalized coordinate system. Three-dimensional unsteady N-S equation in a generalized coordinate system can be written as

$$\frac{\partial \hat{q}}{\partial t} + \frac{\partial \hat{E}}{\partial \xi} + \frac{\partial \hat{F}}{\partial \eta} + \frac{\partial \hat{G}}{\partial \zeta} = \frac{\partial \hat{E}_{v}}{\partial \xi} + \frac{\partial \hat{F}_{v}}{\partial \eta} + \frac{\partial \hat{G}_{v}}{\partial \zeta}, \tag{1}$$

where \hat{q} is the vector of conserved variables. \hat{E} , \hat{F} , \hat{G} and \hat{E}_{v} , \hat{F}_{v} , \hat{G}_{v} are inviscid and viscid flux in (x,y,z) directions with respect to generalized coordinate system respectively. t is time.

Spalart-Allmaras (S-A) one-equation model is used for turbulence enclosure and constructing hybrid RANS/LES method. Second order central difference scheme are used for viscid flux discretization. Linearized Euler implicit form is adopted for time discretization and diagonalized alternating direction implicit (DADI) method is adopted for time advancing. Dual-time stepping method is adopted to solve unsteady flow field.

2.2 WENO-K Spatial Discretization Scheme

In this paper, WENO-K scheme with high order and low dissipation is adopted as spatial discretization scheme. WENO-K scheme proposed by Han et al [11] can reduce dissipation in smooth regions while preserving high-resolution around discontinuities. The WENO-K scheme adopts a Kriging model with non-polynomial Gauss exponential function to obtain new reconstruction coefficients that contain a hyper-parameter. By adaptively optimizing the hyper-parameter and automatically identifying troubled cells, WENO-K can improve the accuracy of interface reconstruction and significantly reduce the numerical dissipation with small additional computational cost [12].

The reconstruction of the primitive variables $\mathbf{Q} = [\rho, u, v, w, p]^T$ are conducted by using fifth-order WENO-K scheme. Assuming $q_{L,i+1/2}$ is a scalar component of $\mathbf{Q_{L,i+1/2}}$, the 5^{th} -order WENO-K interpolation can be expressed as

$$q_{L,i+1/2} = \omega_0 q_{i+1/2}^{(0)} + \omega_1 q_{i+1/2}^{(1)} + \omega_2 q_{i+1/2}^{(2)}, \tag{2}$$

where $q_{i+1/2}^{(k)}(k=0,1,2)$ are the extrapolated values obtained from cell averages \overline{q} in the k^{th} -order (only 3^{rd} -order for WENO-JS) sub stencil $S_k=(i-k,i-k+1,i-k+2)$ and are given by

$$\begin{cases} q_{i+1/2}^{(0)} = (\frac{1}{3} - \frac{1}{4}\theta)\overline{q}_{i-2} + (-\frac{7}{6} + 3\theta)\overline{q}_{i-1} + (\frac{11}{6} - \frac{11}{4}\theta)\overline{q}_{i} \\ q_{i+1/2}^{(1)} = (-\frac{1}{6} - \frac{1}{4}\theta)\overline{q}_{i-1} + (\frac{5}{6} - \frac{1}{3}\theta)\overline{q}_{i} + (\frac{1}{3} + \frac{7}{12}\theta)\overline{q}_{i+1} \\ q_{i+1/2}^{(2)} = (\frac{1}{3} + \frac{7}{12}\theta)\overline{q}_{i} + (\frac{5}{6} - \frac{1}{3}\theta)\overline{q}_{i+1} + (-\frac{1}{6} - \frac{1}{4}\theta)\overline{q}_{i+2}, \end{cases}$$
(3)

where the interpolation coefficients containing θ is a simplification for results of Gauss-Kriging interpolation, and θ is the hyper-parameter involved by Gauss basis function, which needs to be optimized to enhance the accuracy of reconstruction. After a series of complex error analysis, the optimized hyper-parameter can be expressed as

$$\theta = \frac{6}{5} \frac{\overline{q}_{i-1} - 3\overline{q}_i + 3\overline{q}_{i+1} - \overline{q}_{i+2}}{\overline{q}_{i-1} - 15\overline{q}_i + 15\overline{q}_{i+1} - \overline{q}_{i+2}}.$$
(4)

It is obvious that the WENO-K scheme degenerates to WENO-JS scheme when the value of θ equals to 0. Three three-cell stencils are combined with nonlinear weights $\omega_k(k=0,1,2)$ to form an interpolation with higher than fifth order. The expressions of nonlinear weights ω_k are given by

$$\omega_k = \frac{\alpha_k}{\alpha_0 + \alpha_1 + \alpha_2},\tag{5}$$

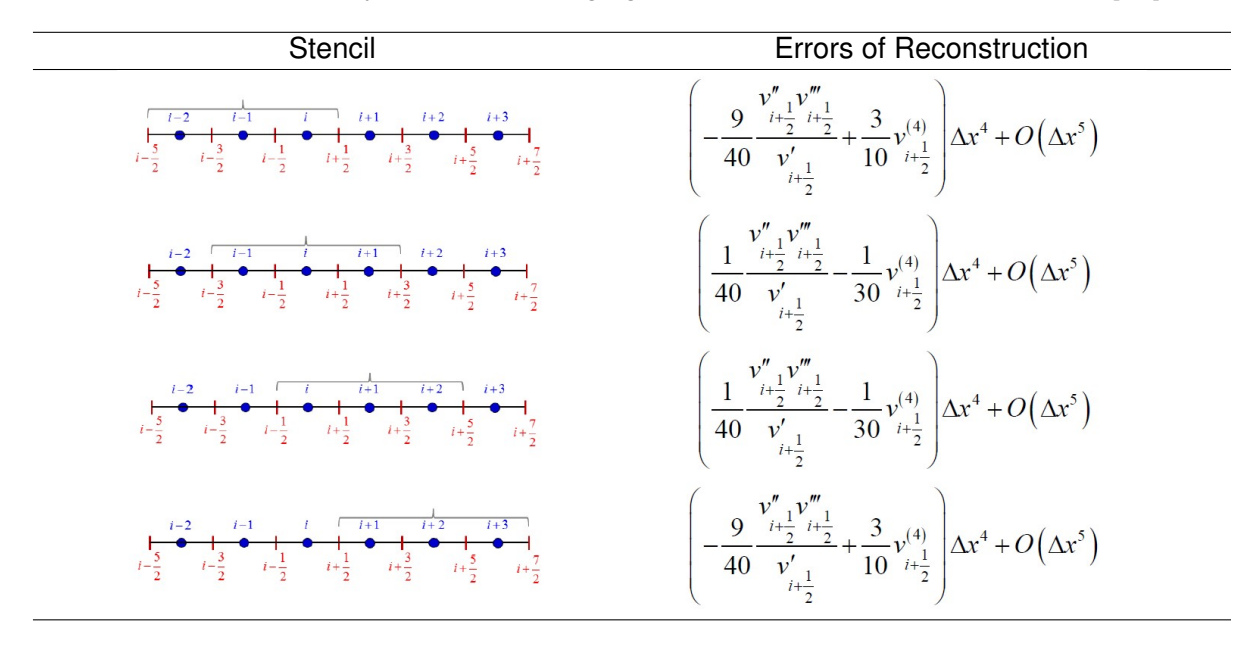
$$\alpha_k = \frac{C_k}{\varepsilon + IS_k},\tag{6}$$

where $C_0 = 0.1, C_1 = 0.6, C_2 = 0.3, \varepsilon = 1 \times 10^{-6}$. IS_k are the 'smoothness indicators' of the stencil S_k which are the same as that of the WENO-JS scheme.

The right value $q_{R,i+1/2}$ can be obtained by symmetry of the left and right states. After Cartesian coordinate system (x,y,z) is transformed to curvilinear coordinate system (ξ,η,ζ) , spatial dimensions can be approximately decoupled and the reconstruction can be performed efficiently dimension by dimension.

Table 1 shows the reconstruction precision of the 5^{th} -order WENO-K scheme, which can achieve 4^{th} -order while traditional 5^{th} -order WENO-JS scheme can only achieve 3^{rd} -order under the same sub-stencil. For strict theoretical derivation, see Ref [11].

Table 1 – Error analysis of Gauss-Kriging reconstruction on three-cell stencils [11]



2.3 S-A IDDES Method

Improved Delayed Detached Eddy Simulation (IDDES) method [13] is a kind of DES method which combines Delayed Detached Eddy Simulation (DDES) [14] with Wall Modelling Large Eddy Simulation (WMLES) [15]. IDDES method can strike a balance between computational efficiency and simulation accuracy, which is especially suitable for the simulation of complex flow problems. S-A IDDES is constructed by defining a new hybrid turbulence length-scale L_{IDDES} , which is composed of RANS lenth-scale L_{RANS} and LES length-scale L_{LES} . L_{IDDES} can be expressed as

$$L_{IDDES} = f_{hyb}(1 + f_{restore})L_{RANS} + (1 - f_{hyb})L_{LES}.$$
(7)

where f_{hyb} is hybrid function, $f_{restore}$ is an empirical function to solve Log-Layer Mismatch (LLM) problem. For S-A RANS turbulence model, the length-scale L_{RANS} is equal to the distance to the wall, i.e. $L_{RANS} = d_w$. L_{LES} is defined according to the subgrid length-scale Δ as

$$L_{LES} = C_{DES} \Psi \Delta. \tag{8}$$

 C_{DES} is the the fundamental empirical constant of DES [16] and Ψ is an introduced low-Reynolds number correction in order to compensate the activation of the low-Reynolds number terms of some background RANS model in LES mode. For S-A RANS turbulence model:

$$C_{DES} = 0.65,$$
 (9)

$$\Psi^{2} = min \left\{ 10^{2}, \frac{1 - \frac{c_{b1}}{c_{w1} \kappa^{2} f_{w}^{*}} [f_{t2} + (1 - f_{t2}) f_{v2}]}{f_{v1} max (10^{-10}, 1 - f_{t2})} \right\}, \tag{10}$$

where all the notations, except for the quantity $f_w^* = 0.424$, are the same as that in the S-A RANS model [17]. In IDDES method, the subgrid length-scale Δ is redefined as

$$\Delta = \min\{\max[C_w d_w, C_w h_{max}, h_{wn}], h_{max}\},\tag{11}$$

where h_{wn} is the local grid scale of grid cells in the normal direction of walls. C_w is a constant, usually equals to 0.15. h_{max} is the maximum length in three directions of grid cells. The definition of Δ includes not only the local grid scale but also the influence of wall distance.

 f_{hvb} is the hybrid function that has 2 branches, DDES branch and WMLES branch:

$$f_{hyb} = max\{(1 - f_{dt}), f_{step}\}.$$
 (12)

 f_{dt} is the delaying function defined in DDES method:

$$f_{dt} = 1 - tanh[(8r_{dt})^3]. (13)$$

The quantity r_{dt} comes from S-A RANS turbulence model. f_{step} only works when the WMLES model is activited, it makes RANS convert to LES in boundary layer. f_{step} can be expressed as

$$f_{step} = min\{2e^{(-9\alpha)^2}, 1.0\},\tag{14}$$

where $\alpha = 0.25 - d_w/h_{max}$. The value of f_{step} ranges from 0 to 1. When $0.5h_{max} < d_w < h_{max}$, it can transform RANS ($f_{step} = 1.0$) method to LES ($f_{step} = 0.0$) method.

The function $f_{restore}$ is used to prevent the RANS Reynolds stress from decreasing too rapidly near the interface between the RANS solution region and the LES solution region. $f_{restore}$ can be expressed as:

$$f_{restore} = max\{(f_{hill} - 1, 0)\}f_{amp}$$

$$\tag{15}$$

where f_{hill} is defined as:

$$f(x) = \begin{cases} 2e^{-11.09\alpha^2} & , \alpha \ge 0\\ 2e^{-9.0\alpha^2} & , \alpha < 0 \end{cases}$$
 (16)

Function f_{amp} is defined as:

$$f_{amp} = 1.0 - max\{f_t, f_1\} \tag{17}$$

where $f_t = tanh[(c_t^2 r)^3]$, $f_l = tanh[(c_l^2 r)^{10}]$. For S-A model, $c_l = 3.55$, $c_t = 1.63$.

3. Validation of Simulation Method of Airfoil in Reverse Flow

The simulation method is validated against experiment of NACA 0012 airfoil in reverse flow [1]. The chimera grid of NACA 0012 airfoil is shown in Figure 2. The near-body O-grid (shown in Figure 2a) has 489 points in the circumferential direction and 149 points in the normal direction. Isotropic grids are generated in the leeward region and wake region to better simulate the large separation flow. The grid spacing at the wall is chosen to ensure $y^+ \approx 0.5$ in the first cell, with approximately 50 points resolving the boundary layer. This grid distribution method is recommended in [10] [18] and is found to be quite important for accurately predicting reverse flow phenomena. The spanwise length is 2C and the spanwise layer is 100. Far field distance is 50C. The number of near-body grid is 10,530,126 and the total number of the chimera grid is 17,069,731.

The free stream velocity is $V_{free}=22.7m/s$, Reynolds number is $Re=1.1\times10^5$. S-A IDDES method and 5^{th} -order WENO-K scheme are applied in CFD calculation. Time step is $C/(200V_{free})$. Calculate 40 cycles and take the average of the force and moment coefficients for the last 10 cycles as the results. The results are shown in Figure 3. Figures show that the results of URANS and IDDES method are in good agreement with the experimental values at small angles of attack, but when the angle of attack reaches $\alpha_{rev}=-10^\circ$, the lift and drag calculated by URANS method are smaller than the experiment values, while IDDES method can still accurately calculate the force and moment coefficient.

Due to the lack of pressure coefficient in Lind's test, Pope's wind tunnel experiment of NACA 0015 airfoil [3] is selected and Smith's URANS CFD results [9] are also used for comparison. The grid generation method and simulation method are the same as that of NACA 0012 airfoil mentioned above. Reynolds number of NACA 0015 airfoil in reverse flow is 1,230,000. The results are shown in

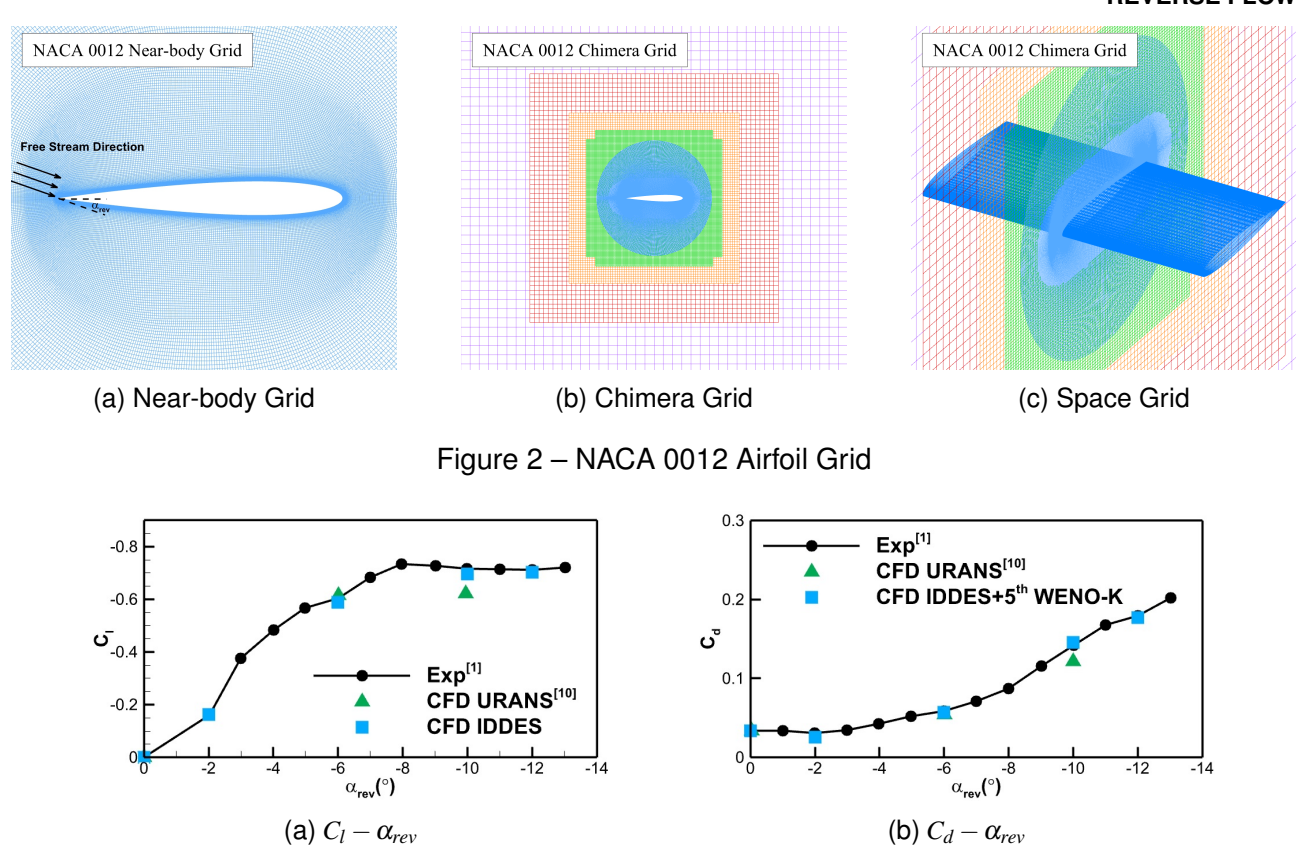


Figure 3 – NACA 0012 Airfoil Force coefficient

Figure 4. The pressure coefficient distribution of URANS method differs greatly from the experiment values on the lower surface, which indicates URANS method cannot capture the complex vortex structure where large separation pccurs. While the results of IDDES method are in good agreement with the experimental results in the lower surface.

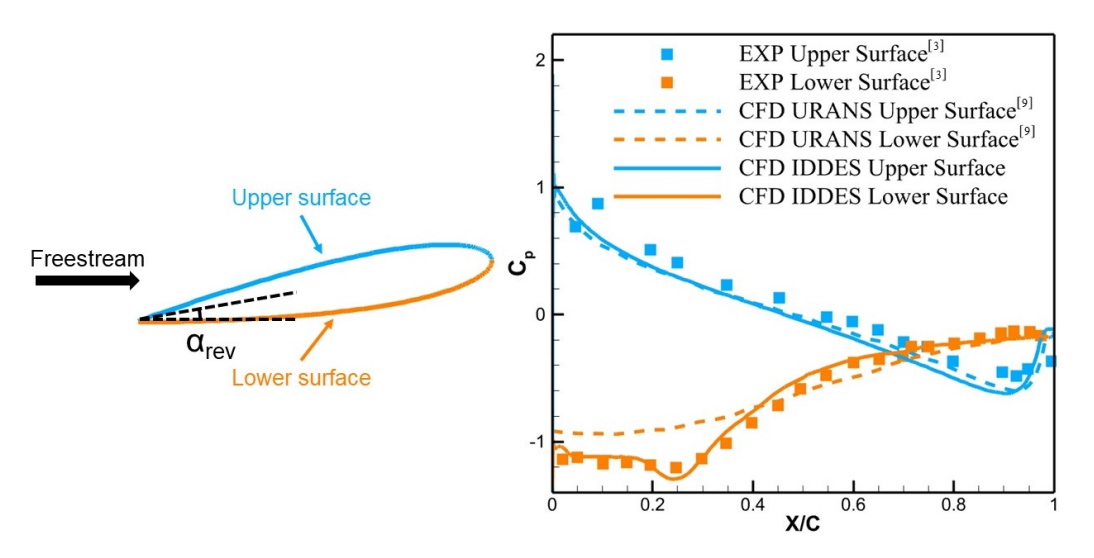


Figure 4 – NACA 0015 Airfoil Pressure Coefficient

Figure 5 shows mean velocity magnitude contours of NACA 0012 airfoil [1] in reverse flow at $\alpha_{rev}=0^{\circ},-6^{\circ},-12^{\circ}$ of CFD simulation and PIV experiment. The results show that the CFD simulation are consistent with the velocity magnitude contours of PIV experiments.

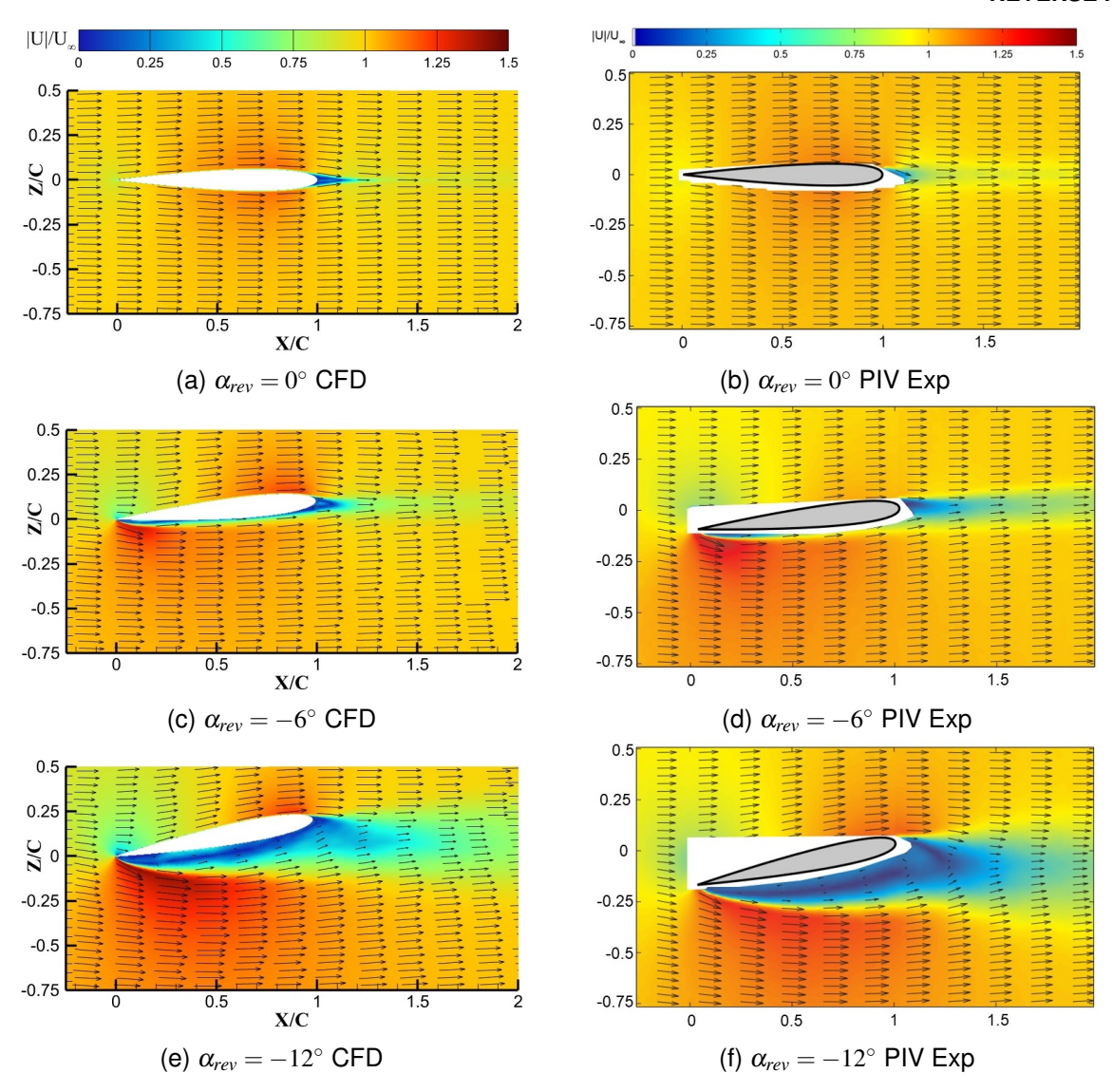


Figure 5 – Comparison between CFD and Experiment of NACA 0012 Airfoil Velocity Contour

In summary, the simulation results of the validation examples are consistent in terms of aerodynamic force/moment coefficient, pressure distribution, and velocity magnitude contours. Therefore, it is believed that the simulation method used in this paper can accurately capture the flow characteristics of rotor airfoils in reverse flow.

4. Results

In order to study the effects of geometry parameters on aerodynamic characteristics of rotor airfoil in reverse flow, OA312 rotor airfoil is selected as a baseline and morphed by an airfoil parameterization and modification method with different geometry parameters, including leading-edge radius, trailing-edge shape, camber, camber crest position, thickness, thickness crest position. Then the aerodynamic coefficients of these modified airfoils are simulated and compared to analyze the influence of different geometry parameters. The geometric morphing method and conclusions are introduced in the following section.

4.1 Airfoil Parameterization Modification

In order to obtain airfoils with different geometry parameters, an airfoil parameterization and modification method (PARFOIL) developed by Lim [19] is used to modify the geometry parameters of the base airfoil. PARFOIL includes eight parameters - camber, camber crest position, thickness, thickness crest position, leading edge radius, trailing edge camber, trailing edge camber crest position and boat-tail angle. Figure 6 shows diagram of airfoil coordinates with geometry parameters.

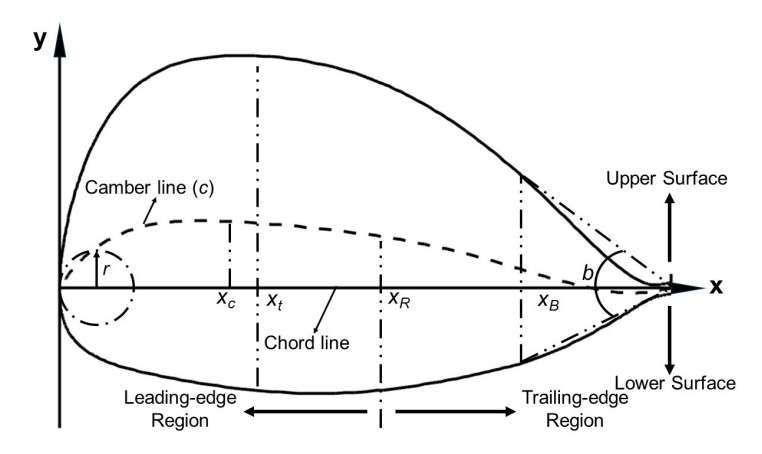


Figure 6 – Diagram of airfoil coordinates with geometry parameters [19]

In this article, only camber, camber crest position, thickness, thickness crest position and leading edge radius are morphed with PARFOIL method. To morph the camber or the thickness of airfoil, the camber or thickness of the morphed airfoil can be obtained by a scaling factor (f_m) times baseline line value (t_{BL}) :

$$t = f_m \cdot t_{BL} \tag{18}$$

The modification of the camber crest position or the thickness crest position can be obtained by a delta value (Δx) of the horizontal coordinate x on the baseline airfoil. An example of changing the camber crest position is given as follows, the thickness crest position can be changed in the same way:

$$x' = x + \Delta x_c \tag{19}$$

where

$$\Delta x_c = C_3(x - x_c)^3 + C_2(x - x_c)^2 + (x_c' - x_c)$$
(20)

$$C_2 = -\frac{(x_c' - x_c)(1 - 3x_c + x_c^2)}{(1 - x_c^2)x_c^2}$$
 (21)

$$C_3 = \frac{(x_c' - x_c)(1 - 2x_c)}{(1 - x_c^2)x_c^2} \tag{22}$$

In the above equation, x_c and x'_c are the camber crest position of the baseline airfoil and the morphed airfoil. Since camber distribution has also been altered, the y-coordinate of the morphed airfoil can be expressed as:

$$y^{u}(x) = \frac{y_{BL}^{u} + y_{BL}^{l}}{2} + t_{BL}^{\prime}$$
 (23)

$$y^{l}(x) = \frac{y_{BL}^{u} + y_{BL}^{l}}{2} - t_{BL}^{\prime}$$
 (24)

where the superscripts u, l means upper surface and lower surface, t'_{BL} means thickness distribution of the morphed airfoil.

The leading-edge radius r of the morphed airfoil can also be obtained with a scaling factor f_k multiplying the baseline value r_{BL} :

$$r = f_r \cdot r_{BL} = \frac{1}{2} a_0^2 \tag{25}$$

Then the thickness of the morphed airfoil's upper surface $y^{u}(x)$ and lower surface $y^{l}(x)$ in the leading-edge region can be expressed as follows:

$$y^{u}(x) = a_0 \sqrt{x} + a_1 x + a_2 x^2 \tag{26}$$

where

$$a_1 = \frac{2t_0}{x_0} - \frac{3}{2} \frac{a_0}{\sqrt{x_0}} \tag{27}$$

$$a_2 = -\frac{t_0}{x_0^2} + \frac{a_0}{2x_0^{3/2}} \tag{28}$$

In the above expressions, a_0 is calculated in Eq.(25), and t_0 is the corresponding thickness at the thickness crest position (x_t) . The thickness of the morphed airfoil's lower surface can be calculated using Eq.(27)

To study the effect of rotor airfoil's geometry parameters on aerodynamics characteristic in reverse flow, leading-edge radius (LR), camber (C), camber crest position (CP), thickness (T), thickness crest position (TP) and trailing-edge shape of a baseline OA312 airfoil are morphed. A series of modified airfoils with different geometry parameters are obtained by using the PARFOIL method mentioned in Section 4.1. Figure 7 shows baseline OA312 airfoil and modified airfoils. The number in the name of morphed airfoils indicates the geometry parameter as a percentage of the chord length, such as OA312-LR0.7 means the leading-edge radius of the airfoil is morphed into 0.7%C.

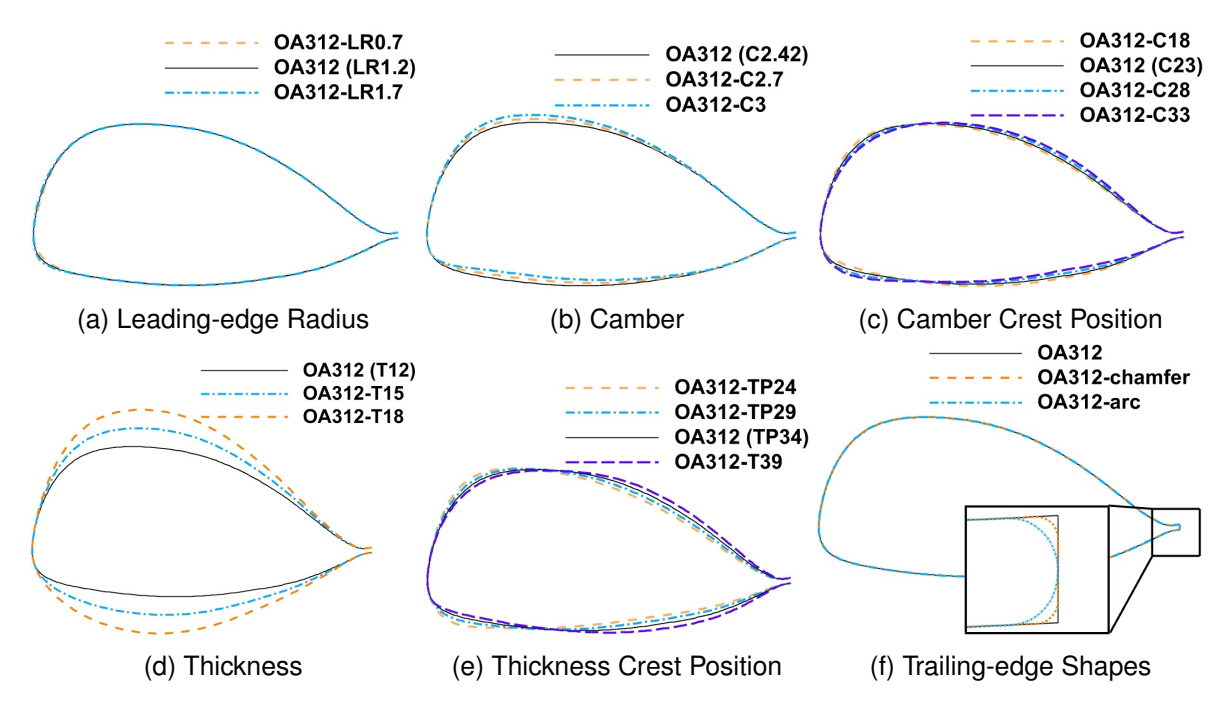


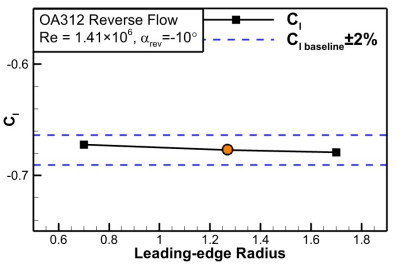
Figure 7 - OA312 and its morphed airfoils

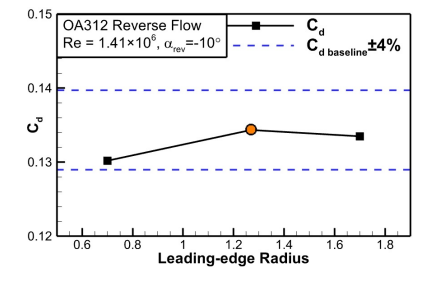
The simulation condition of baseline OA312 airfoil and other morphed airfoils is: $Re_c = 1.41 \times 10^6$, $\alpha_{rev} = -10^\circ$. All of the CFD simulation below are conducted in this condition.

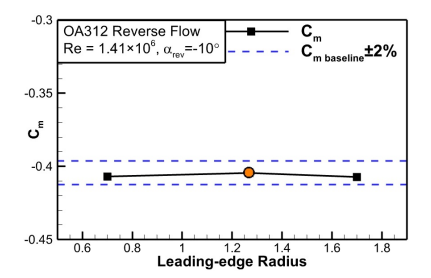
4.2 Influence of airfoil's leading-edge radius and trailing-edge shape on aerodynamic characteristics of rotor airfoil in reverse flow

4.2.1 Leading-edge Radius

The simulation results of airfoils with different leading-edge radius are shown in Figure 8. The deviation of lift, moment coefficient are within 2% of that of the baseline airfoil and the deviation of drag coefficient are within 4% of that of the baseline airfoil. The figures shows that leading-edge radius hardly ever influence the aerodynamics characteristic in reverse flow. It is easy to explain this phenomenon: in reverse flow leading-edge becomes aerodynamic trailing-edge which is far from the incoming free stream, thus it has negligible effects on the aerodynamics characteristics.







(a) C_l .vs. Leading-edge Radius

(b) C_d .vs. Leading-edge Radius

(c) C_m .vs. Leading-edge Radius

Figure 8 - Leading-edge Radius

4.2.2 Trailing-edge Shape

The simulation results of airfoils with different trailing-edge shapes are shown in Figure 2. The drag of an airfoil with arc-shape or chamfer-shape trailing-edge is reduced by 6.8% and 7.1% respectively. The negative lift of OA312-arc airfoil is less than baseline airfoil, but the negative lift of OA312-chamfer is larger than baseline airfoil. Both of the airfoils' moment characteristic deteriorate.

Table 2 – Trailing-edge Shapes

Airfoil	C_l	C_d	C_m
OA312	-0.6772	0.1344	-0.4044
OA312-arc	-0.6617	0.1252	-0.4158
OA312-chamfer	-0.6899	0.1248	-0.4251

The drag reduction mechanism of changing the trailing-edge shape can also be analyzed from separation weakening. Figure 9 shows streamlines of OA312, OA312-arc and OA312-chamfer airfoils. It is obvious that flow separation of airfoils with morphed trailing-edge shape is weaken. The separation bubbles are smaller and the pressure drag of airfoils decrease (see Table 3).

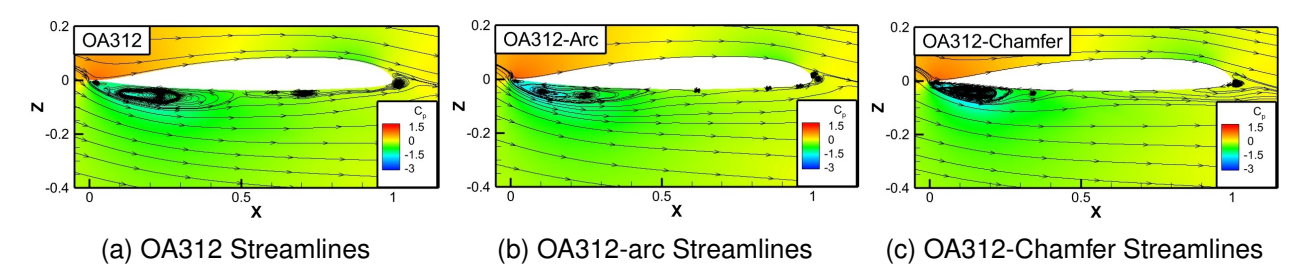


Figure 9 – Effect of Trailing-edge Shape on Streamlines

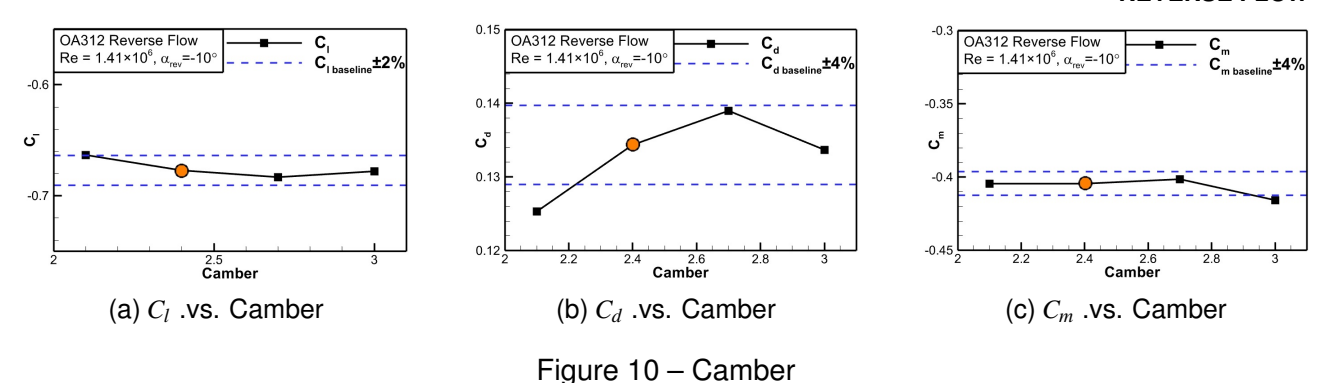
Table 3 - Drag Decomposition

Airfoil	OA312	OA312-arc	OA312-chamfer
Total Drag	0.1344	0.1252	0.1248
Viscous Drag	0.0029	0.0032	0.0030
Pressure Drag	0.1315	0.1220	0.1218

4.3 Influence of airfoil's camber and camber crest position on aerodynamic characteristics of rotor airfoil in reverse flow

4.3.1 Camber

The simulation results of airfoils with different camber are shown in Figure 10. It can be seen from the figures that camber has little effect on aerodynamics characteristic in reverse flow. With the change of airfoil's camber, the lift coefficient and moment coefficient change about 2% and the drag coefficient change about 4% compared with that of the baseline airfoil.



4.3.2 Camber Crest Position

The simulation results of airfoils with different camber crest position are shown in Figure 11. It can be seen from the figures that camber crest position has little effect on drag coefficient. However, camber crest position can reduce negative lift and pitching moment caused by reverse flow. Negative lift and pitching moment decrease with camber crest position moving backward (Figure 11a and Figure 11c).

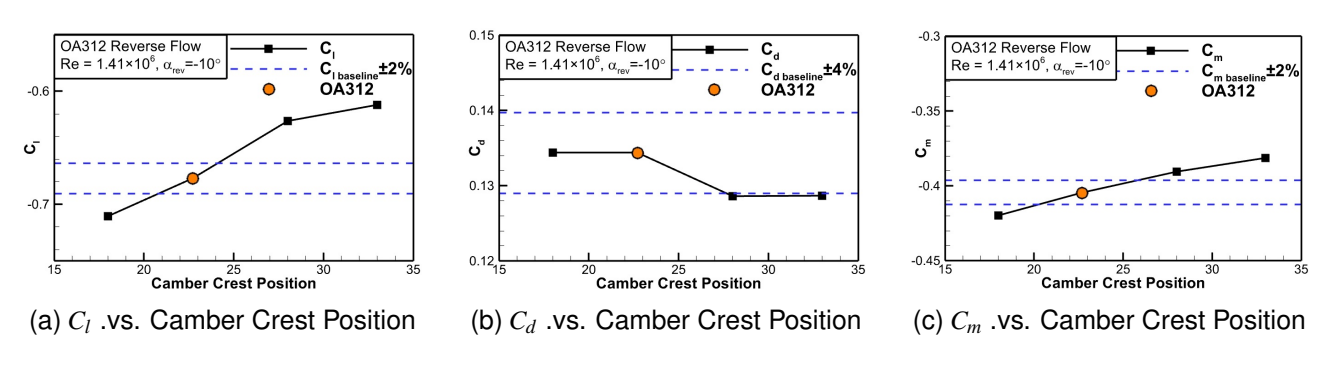


Figure 11 - Camber Crest Position

Figure 12 shows pressure coefficient distribution curve. It can be seen from the figure that the platform region (marked by red square in Figure 12) of morphed airfoils with camber crest position nearer to leading-edge is lower than baseline airfoil and OA312-CP18. This phenomenon indicates that airfoils with the rear camber crest position has a smaller pressure drop due to the separation of the trailing-edge in reverse flow. Therefore, the negative lift of the airfoil is also smaller.

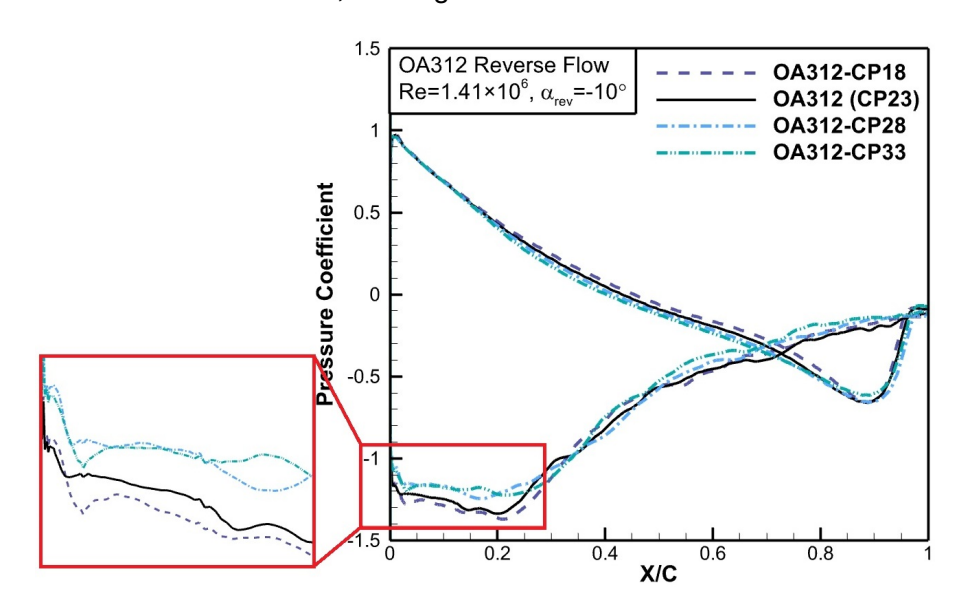


Figure 12 – Pressure Coefficient Distribution Curve

4.4 Influence of airfoil's thickness and thickness crest position on aerodynamic characteristics of rotor airfoil in reverse flow

4.4.1 Thickness

The simulation results of airfoils with different thickness are shown in Figure 13. It can be seen from the figure that thickness has little effect on lift coefficient. With airfoil's thickness increasing, the drag coefficient decreases but the moment coefficient increases.

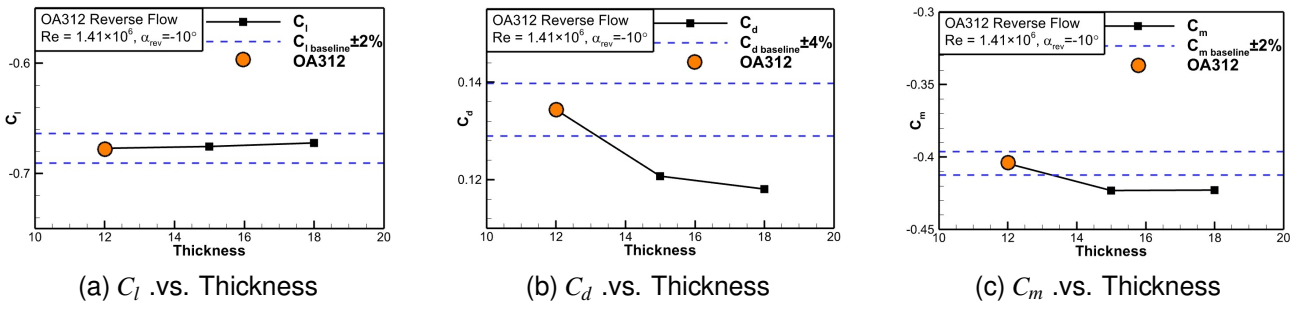


Figure 13 - Thickness

The drag reduction mechanism of increase airfoils' thickness can also be analyzed from separation weakening. Figure 14 shows streamlines of OA312, OA312-T15 and OA312-T18 airfoils. It is obvious that the separation of the airfoils with increased thickness is weaken. The separation bubbles are smaller so the pressure drag of airfoils decreases.

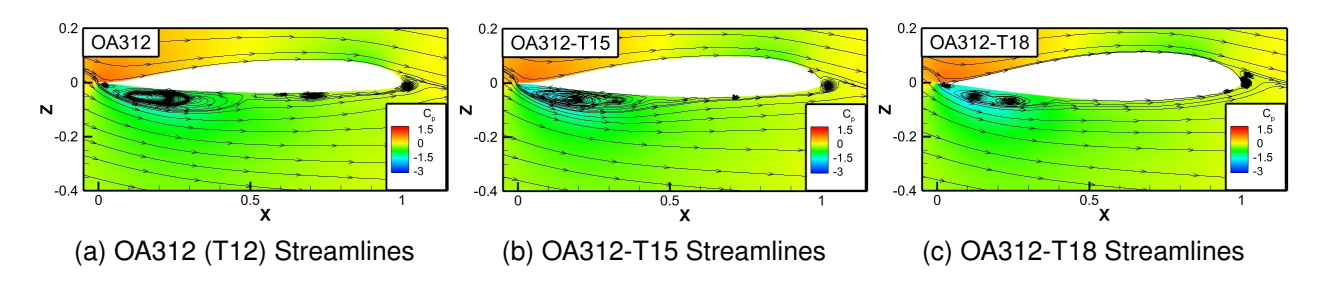


Figure 14 – Effect of Thickness on Streamlines

4.4.2 Thickness Crest Position

The simulation results of airfoils with different thickness crest position are shown in Figure 15. It can be seen from the figure that thickness crest position has little effect on lift and moment coefficient. With the airfoil's thickness crest position moving to trailing-edge, the drag coefficient decreases.

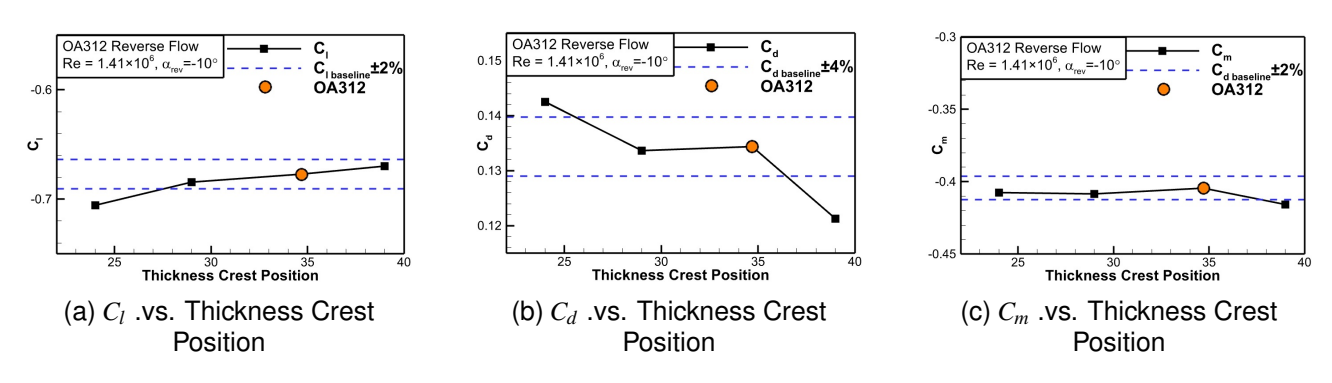


Figure 15 – Thickness Crest Position

The drag reduction mechanism of increase airfoils' thickness crest position can also be analyzed from separation weakening. Figure 16 shows streamlines of OA312-TP24, OA312-TP29, OA312 and OA312-TP39 airfoils. It is obvious that the separation of the airfoils with rear thickness crest position is weaken. The separation bubbles are smaller so the pressure drag of airfoils decreases.

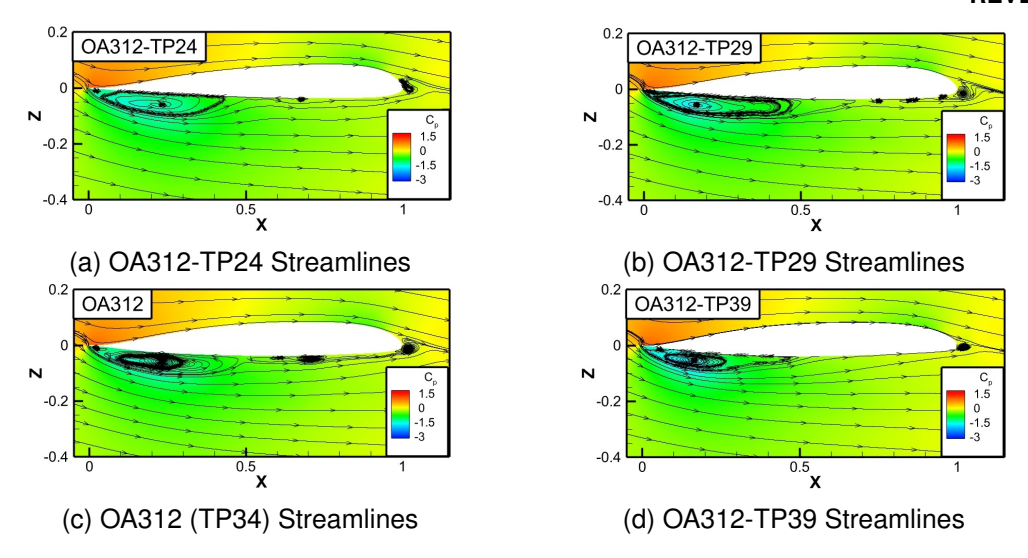


Figure 16 – Effect of Thickness Crest Position on Streamlines

4.5 Summery

Geometry parameter's effect on aerodynamics characteristic in reverse flow is summarized in Table 4. The following conclusion can be drawn from Table 4:

- (1) Except for camber crest position and trailing-edge's shape, most geometry parameters has negligible effect on lift in reverse flow. Increase camber crest position or change trailing-edge shape into arc can reduce negative lift.
- (2) Thickness has a great effect on drag in reverse flow. Decrease airfoil thickness and thickness crest position can reduce drag. Change trailing-edge shape into arc or chamfer can also reduce drag.
- (3) Thickness and camber crest position effect pitching moment. Increase camber crest position or decrease airfoil thickness can reduce pitching moment.

Geometry Parameter $-C_l$ C_d $|C_m|$ Leading-edge Radius Camber Camber Crest Position $-C_l/C_d/|C_m|$ decrease with **Thickness** parameter decreasing Thickness Crest Position $-C_l/C_d/|C_m|$ decrease with parameter increasing Trailing-edge Arc Parameter's effect on Trailing-edge Chamfer $-C_{l}/C_{d}/|C_{m}|$ is neglected

Table 4 – Geometry parameter's effect on aerodynamics characteristic in reverse flow

5. Conclusion

In this paper a high-accurate numerical simulation of vortex-dominated flow over rotor airfoil is conducted by using fifth-order WENO-K scheme and IDDES method and effect of rotor airfoil's geometry parameters on aerodynamics characteristic in reverse flow is studied:

(1) The results of URANS and IDDES simulation indicate that using the high-order and low-dissipation WENO-K scheme to discrete inviscid flux can improve the computational accuracy of aerodynamic characteristics in reverse flow.

- (2) To improve rotor airfoil's lift characteristic in reverse flow, camber crest position can be moved backward or trailing-edge's shape can be morphed into arc. The mechanism of reduce negative lift is decreasing pressure drop caused by the separation of sharp trailing-edge.
- (3) To improve rotor airfoil's drag characteristic in reverse flow, decreasing airfoil thickness or moving thickness crest position forward can be applied in rotor airfoil design. The mechanism of drag reduction is reducing separation near trailing-edge so as to reduce pressure drag caused by separation.
- (4) To improve rotor airfoil's moment characteristic in reverse flow, increasing camber crest position or decreasing airfoil thickness can be applied in rotor airfoil design.

6. Acknowledgement

This work was supported by the National Key Research and Development Program of China under Grant No. 2023YFB3002800.

7. Contact Author Email Address

Wen-Ping Song*, Professor, wpsong@nwpu.edu.cn, corresponding author

8. Copyright Statement

The authors confirm that they, and/or their company or organization, hold copyright on all of the original material included in this paper. The authors also confirm that they have obtained permission, from the copyright holder of any third party material included in this paper, to publish it as part of their paper. The authors confirm that they give permission, or have obtained permission from the copyright holder of this paper, for the publication and distribution of this paper as part of the ICAS proceedings or as individual off-prints from the proceedings.

References

- [1] Andrew H. Lind, Jonathan N. Lefebvre, and Anya R. Jones. Experimental Investigation of Reverse Flow over Sharp and Blunt Trailing Edge Airfoils. In *31st AIAA Applied Aerodynamics Conference*, Fluid Dynamics and Co-located Conferences. American Institute of Aeronautics and Astronautics, June 2013.
- [2] George Jacobellis, Farhan Gandhi, Thomas Rice, and Michael Amitay. Computational and Experimental Investigation of Camber-Morphing Airfoils for Reverse Flow Drag Reduction on High-Speed Rotorcraft. *Journal of the American Helicopter Society*, 65, January 2019.
- [3] Alan Pope. The Forces and Pressures over an NACA 0015 Airfoil Through 180 Degrees Angle of Attack. Technical report, Georgia Institute of Technology, 1949.
- [4] J. Gordon Leishman. Aerodynamic Characteristics of a Helicopter Rotor Airfoil as Affected by Simulated Ballistic Damage. Technical report, University of Maryland, Department of Aerospace Engineering College Park, Maryland, December 1993.
- [5] Andrew H. Lind, Jonathan N. Lefebvre, and Anya R. Jones. Time-Averaged Aerodynamics of Sharp and Blunt Trailing-Edge Static Airfoils in Reverse Flow. *AIAA Journal*, 52(12):2751–2764, December 2014. Publisher: American Institute of Aeronautics and Astronautics.
- [6] Andrew H. Lind and Anya R. Jones. Vortex Shedding from Airfoils in Reverse Flow. *AIAA Journal*, 53(9):2621–2633, September 2015. Publisher: American Institute of Aeronautics and Astronautics.
- [7] Andrew H. Lind and Anya R. Jones. Unsteady airloads on static airfoils through high angles of attack and in reverse flow. *Journal of Fluids and Structures*, 63:259–279, May 2016.
- [8] Andrew H. Lind, Luke R. Smith, Joseph I. Milluzzo, and Anya R. Jones. Reynolds Number Effects on Rotor Blade Sections in Reverse Flow. *Journal of Aircraft*, 53(5):1248–1260, September 2016. Publisher: American Institute of Aeronautics and Astronautics.
- [9] Marilyn J. Smith, Nicholas D. Liggett, and Benjamin C. G. Koukol. Aerodynamics of Airfoils at High and Reverse Angles of Attack. *Journal of Aircraft*, 48(6):2012–2023, 2011. Publisher: American Institute of Aeronautics and Astronautics _eprint: https://doi.org/10.2514/1.C031428.
- [10] Joachim Hodara, Andrew H. Lind, Anya R. Jones, and Marilyn J. Smith. Collaborative Investigation of the Aerodynamic Behavior of Airfoils in Reverse Flow. *Journal of the American Helicopter Society*, 61(3):1–15, July 2016.
- [11] Shao-Qiang Han, Wen-Ping Song, and Zhong-Hua Han. An improved WENO method based on Gauss-kriging reconstruction with an optimized hyper-parameter. *Journal of Computational Physics*, 422:109742, December 2020.
- [12] Shaoqiang HAN, Wenping SONG, and Zhonghua HAN. A novel high-order scheme for numerical simulation of wake flow over helicopter rotors in hover. *Chinese Journal of Aeronautics*, 35(5):260–274, 2022.
- [13] Mikhail L. Shur, Philippe R. Spalart, Mikhail Kh. Strelets, and Andrey K. Travin. A hybrid RANS-LES approach with delayed-DES and wall-modelled LES capabilities. *International Journal of Heat and Fluid Flow*, 29(6):1638–1649, December 2008.
- [14] P. R. Spalart, S. Deck, M. L. Shur, K. D. Squires, M. Kh. Strelets, and A. Travin. A New Version of Detached-eddy Simulation, Resistant to Ambiguous Grid Densities. *Theoretical and Computational Fluid Dynamics*, 20(3):181–195, July 2006.
- [15] K. Abe. A hybrid LES/RANS approach using an anisotropy-resolving algebraic turbulence model. *International Journal of Heat and Fluid Flow*, 26(2):204–222, 2005.
- [16] M. Shur, P. R. Spalart, M. Strelets, and A. Travin. Detached-eddy simulation of an airfoil at high angle of attack. In W. Rodi and D. Laurence, editors, *Engineering Turbulence Modelling and Experiments 4*, pages 669–678. Elsevier Science Ltd, Oxford, 1999.
- [17] P. Spalart and S. Allmaras. A one-equation turbulence model for aerodynamic flows. In *30th Aerospace Sciences Meeting and Exhibit*, Reno,NV,U.S.A., January 1992. American Institute of Aeronautics and Astronautics.
- [18] Yue Wang, Kang Liu, Wen-Ping Song, and Zhong-Hua Han. Scale-Adaptive Simulations of Unsteady Flow around NACA0021 Airfoil at 60^{*} angle of attack. In *AIAA Scitech 2019 Forum*, AIAA SciTech Forum. American Institute of Aeronautics and Astronautics, January 2019.
- [19] Joon Lim. Application of Parametric Airfoil Design for Rotor Performance Improvement. In *44th European Rotorcraft Forum*, Delft, Netherlands, February 2022.